

Performance Analysis of a High-Order Discontinuous Galerkin Method Application to the Reverse Time Migration

Caroline Baldassari^{1,2,*}, H el ene Barucq^{1,2}, Henri Calandra³,
Bertrand Denel³ and Julien Diaz^{1,2}

¹ INRIA Bordeaux Research Center, Project Team Magique3D, Avenue de l'universit e,
64013 Pau Cedex, France.

² LMA, CNRS UMR 5142, Universit e de Pau, Avenue de l'universit e, 64013 Pau
Cedex, France.

³ TOTAL, Avenue Larribau, 64000 Pau, France.

Received 29 December 2009; Accepted (in revised version) 17 December 2010

Available online 24 October 2011

Abstract. This work pertains to numerical aspects of a finite element method based discontinuous functions. Our study focuses on the Interior Penalty Discontinuous Galerkin method (IPDGM) because of its high-level of flexibility for solving the full wave equation in heterogeneous media. We assess the performance of IPDGM through a comparison study with a spectral element method (SEM). We show that IPDGM is as accurate as SEM. In addition, we illustrate the efficiency of IPDGM when employed in a seismic imaging process by considering two-dimensional problems involving the Reverse Time Migration.

AMS subject classifications: 65M12, 65M60, 35L05

Key words: Interior penalty discontinuous Galerkin method, spectral element method, reverse time migration, seismic imaging process.

1 Introduction

Oil exploration is still an ongoing activity in spite that the new target regions are difficult to access (hostile climate and geography). Prior to drilling, it is thus very important to have a reliable prediction tool such as depth imaging. This produces an image in the manner of an ultrasound using artificial seismic waves caused by explosive sources. The

*Corresponding author. *Email addresses:* caroline.baldassari@inria.fr (C. Baldassari), helene.barucq@inria.fr (H. Barucq), henri.calandra@total.com (H. Calandra), bertrand.denel@total.com (B. Denel), julien.diaz@inria.fr (J. Diaz)

waves that are reflected by heterogeneities of the medium are then recorded by receivers which are positioned in advance to cover a reasonable area to explore. The receivers are capable of recording both the arrival times and amplitudes of the reflected waves. Arrival time, which are directly associated with medium velocities, are used to produce a map of the reflectors depicting the interfaces between different media. Amplitudes are related to the properties of the materials constituting the subsurface. In most cases, the map obtained by depth imaging represents only the interfaces and the produced image is called the velocity model. The initialization of the imaging process is carried out in a campaign of acquisition that records the reflected waves generated by the propagation of seismic sources. The image is then obtained by reproducing the propagation of seismic wave fields numerically. Producing an accurate image may require several iterations of this process. Seismic imaging can therefore be viewed as an iterative method which requires, at each step, solving the wave equation twice (propagation and back propagation). Therefore, seismic imaging techniques depend on both the wave equation model and on the numerical method. When using the full wave equation, the imaging method is called Reverse Time Migration (RTM). For years, the RTM has been neglected mainly due to algorithmic issues and computing platforms limitations.

To alleviate this difficulty, various methods based on approximated wave equations have been suggested (see for example [11, 14, 18]). These methods do not require significant computing resources. The Phase-Shift method [11, 14] provides an exact solution of the one-way equation when the velocity does not vary laterally. The Split-Step Fourier method [18] can be applied even when the velocity varies in all directions. It uses the phase-shift operator that is corrected at each iteration to account for changes in the environment. The Split-Step Fourier method is more accurate than the Phase Shift method but requires applying Fourier transforms, which greatly increases the computational burden. In addition, the solution is actually accurate when the velocity variations are small enough, which can be a serious restriction for most situations. With the impressive progress made in the area of scientific computing, it is now possible to apply the RTM using advanced numerical methods such as finite element methods (FEM). Most numerical codes that have been designed for RTM are based on finite difference approximations. Finite differences (FDM) are very popular because they provide an explicit representation of the solution, which avoids the inversion of the mass matrix at each time step. They are efficient but they lead to prohibitive computational cost in the case of complex areas with strong heterogeneities and topography. Consequently, FDM methods can not be candidates for RTM when requiring the solution of the wave equation in an iterative scheme.

Based on unstructured meshes, FEM have all the flexibility required to reproduce correctly the topography of the environment and the geometry of the various subsurface's interfaces. FEM approximations are not only very accurate but they are also able to easily combine different orders of approximations. This important feature reduces the computational cost while maintaining the level of accuracy. Note that FEM methods have been so far rarely used because they often deliver an implicit representation of the solution.

To overcome this difficulty, mass condensation procedures were suggested [3, 13]. These techniques have however the effect of blocking the order of approximation. On the other hand, the spectral element methods (SEM), that are based on the Gauss Lobatto quadrature formula, allow the diagonalization of the mass matrix without affecting the order of convergence. SEM was thus successfully applied to the wave equation [6, 7] and more specifically for problems arising in geophysics [15–17]. We also refer to the recent article [8] which is a very interesting state of the art for finite element techniques applied to the propagation of seismic waves. SEM methods are often applied on meshes with quadrilaterals or hexahedra elements. Such meshes are often hard to generate, particularly when the topography and/or interfaces are complex. Note that SEM methods has been applied to meshes with triangular elements [5]. Nevertheless, its implementation with high-order finite element remains difficult. Moreover, to the best of our knowledge, the transition to 3D has not been possible so far. This is a major drawback of SEM since most mesh generators have been developed for tetrahedra elements.

Recently, a new class of methods, called Discontinuous Galerkin Methods (DGM) emerged. DGM methods employ discontinuous functions, and therefore combine much more easily different level of approximation on a single mesh. Furthermore, DGM can be applied to both hexahedra and tetrahedra elements. The approximate solution is expressed in a quasi-explicit way because the mass matrix is block diagonal even when its entries are evaluated analytically.

The aim of this paper is to show that the Interior Penalty Discontinuous Galerkin Method (IPDGM) is well suited for RTM in heterogeneous media in spite the widespread belief that DGM methods are not competitive. Note that IPDGM has been successfully applied for solving the wave equation [12]. However, this work does not provide a performance assessment of the methods. In addition, it seems that [9] is the only work that compare DGM to SEM. The authors concluded that SEM is more efficient than DGM. This observation is however valid only for regular quadrilaterals covering homogeneous media. We show here (see Section 2) that, using triangular-shaped elements, IPDGM exhibits the same level of performance as SEM, for both homogeneous and heterogeneous media. We conclude that IPDGM is more versatile since it accommodates unstructured meshes with arbitrarily-shaped elements. Last, we apply IPDGM to RTM to highlights its potential efficiency. This numerical experiment is performed in the case where the velocity varies strongly. The results reported in Section 3 show that we can recover all the interfaces of the considered subsurface.

2 Interior penalty discontinuous Galerkin method

2.1 General setting

We consider the problem

$$\begin{cases} \frac{1}{\mu} \frac{\partial^2 u}{\partial t^2} - \nabla \cdot \left(\frac{1}{\rho} \nabla u \right) = g, & \text{in }]0, T[\times \Omega, \\ u = 0, & \text{on }]0, T[\times \Gamma_D, \\ \frac{1}{\sqrt{\mu}} \frac{\partial u}{\partial t} + \frac{1}{\sqrt{\rho}} \nabla u \cdot \mathbf{n} = 0, & \text{on }]0, T[\times \Gamma_{abs}, \\ u(x, z, 0) = 0, \quad \frac{\partial u}{\partial t}(x, z, 0) = 0, & \text{in } \Omega, \end{cases} \quad (2.1)$$

where $T > 0$ is the final time of simulation. Ω is the computational box which is assumed to be a bounded lipschitzian domain of \mathbb{R}^2 with boundary $\partial\Omega$. Γ_D and Γ_{abs} are two subsets of $\partial\Omega$ such that $\bar{\Gamma}_D \cup \Gamma_{abs} = \partial\Omega$ and $\Gamma_D \cap \Gamma_{abs} = \emptyset$. The condition imposed on Γ_D is a Dirichlet condition, whereas the one imposed on Γ_{abs} is a first order absorbing boundary condition. The positive parameters μ and ρ are given as functions defined in Ω and they are related to the propagation velocity c by the relation $c = \sqrt{\mu/\rho}$. In particular, μ is the compressibility modulus and ρ is the density of the propagation medium. The positive function μ is supposed to be piecewise continuous and bounded. The function ρ is supposed to be piecewise differentiable and its differential is supposed to be bounded.

The boundary $\partial\Omega$ is regular enough to define the normal unitary vector n that is outwardly directed to Ω . The propagation of the wavefield u is generated by the source g which is given and the initial data defining u and $\partial u/\partial t$ at $t=0$ are supposed to be zero.

When $g \in C^1(0, T; L^2(\Omega))$, it can be proven that the problem (2.1) admits a unique solution u such that $u \in C^0(0, T; \mathcal{D}_\rho(\Omega))$ and $\partial u/\partial t \in C^0(0, T; H^1(\Omega))$, where

$$\mathcal{D}_\rho(\Omega) = \left\{ v \in H^1(\Omega) \mid \nabla \cdot \left(\frac{1}{\rho} \nabla v \right) \in L^2(\Omega) \right\}.$$

This result can be obtained by applying the semi-group theory. However, for the applications that we deal with, the source g is a finite sum of point sources $(g_i)_{i=1, \dots, N}$ which are regular in time but not in space. Indeed, the evolution of g_i is generally described by a second-order derivative of a Gaussian function at a given point. Basically, the sources g_i we consider are given by $g_i(x, z, t) = \delta_i(x, z) R(t)$, where $\delta_i(x, z)$ represents the Dirac distribution at point (x_i, z_i) and R is a Ricker function. We will give an example later on when we present numerical results. They illustrate the fact that the singularity of the sources does not impact the convergence of pointwise error. Another solution could be to consider a sum of regular functions compactly supported in the disk centered at point (x_i, z_i) with very small radius ε .

2.2 The discretized problem

In the following, \mathcal{T}_h is a partition of Ω composed of triangles K such that $\bar{\Omega} = \cup_{K \in \mathcal{T}_h} \bar{K}$. We denote by h_K the diameter of the element K and by $h = \min_{K \in \mathcal{T}_h} h_K$; E_i is an internal edge defined by two elements K^+ et K^- (i.e. $E_i = \partial K^+ \cap \partial K^-$); \mathbf{n}^\pm are the outward normal

vectors to K^\pm ; v^\pm are the traces of a function v on K^\pm ; \mathcal{E}_i is the set of internal edges; E_D (resp. E_{abs}) is an edge lying on the boundary Γ_D (resp. Γ_{abs}); \mathcal{E}_D (resp. \mathcal{E}_{abs}) is the set of all the edges lying on Γ_D (resp. Γ_{abs}).

We also define the jump and the mean-value of a function v on an internal edge E_i by:

$$[[v]] = v^+ \mathbf{n}^+ + v^- \mathbf{n}^- \quad \text{and} \quad \{\{v\}\} := (v^+ + v^-)/2,$$

and on a external edge E_D by $[[v]] := v \mathbf{n}$ and $\{\{v\}\} := v$, where \mathbf{n} is the outward normal vector of E_D .

We define similarly the jump and the mean-value of a vectorial function \mathbf{q} by:

$$\begin{aligned} [[\mathbf{q}]] &:= \mathbf{q}^+ \cdot \mathbf{n}^+ + \mathbf{q}^- \cdot \mathbf{n}^-, & \{\{\mathbf{q}\}\} &:= (\mathbf{q}^+ + \mathbf{q}^-)/2, & \text{on } E_i; \\ [[\mathbf{q}]] &:= \mathbf{q} \cdot \mathbf{n}, & \{\{\mathbf{q}\}\} &:= \mathbf{q}, & \text{on } E_D. \end{aligned}$$

The finite element space that we use is defined by:

$$V_l^h := \left\{ v \in L^2(\Omega) : v|_K \in P_l(K) \forall K \in \mathcal{T}_h \right\}, \tag{2.2}$$

where $P_l(K)$ is the set of polynomials on the element K which total degree is less or equal to l . This space contains functions which are polynomials locally and it does not require the approximate solution $v_h \in V_l^h$ to be continuous in Ω . By this way, the degree of v_h may be different in each element K , which supplies a local and thus adaptative order approximation technique.

To construct the discretized problem, we first consider the semi-discretized problem: Find $u_h : \bar{I} \times V_l^h \rightarrow \mathbb{R}$ such that:

$$\left(\frac{1}{\mu} \frac{\partial^2 u_h}{\partial t^2}, v_h \right) + b_h \left(\frac{\partial u_h}{\partial t}, v_h \right) + a_h(u_h, v_h) = (g, v_h), \quad \forall v_h \in V_l^h, \quad t \in I \tag{2.3}$$

with zero initial conditions.

The bilinear form b_h defined on $V_l^h \times V_l^h$ reads as:

$$b_h(u_h, v_h) := \sum_{E_{\text{abs}} \in \mathcal{E}_{\text{abs}}} \int_{E_{\text{abs}}} \frac{1}{\sqrt{\mu \rho}} u_h v_h dE, \tag{2.4}$$

and the bilinear form a_h defined on $V_l^h \times V_l^h$ is given by:

$$\begin{aligned} a_h(u_h, v_h) &:= \sum_{K \in \mathcal{T}_h} \int_K \frac{1}{\rho} \nabla u_h \cdot \nabla v_h dx - \sum_{E_i \in \mathcal{E}_i \cup \mathcal{E}_D} \int_{E_i} [[u_h]] \cdot \left\{ \left\{ \frac{1}{\rho} \nabla v_h \right\} \right\} dE \\ &\quad - \sum_{E_i \in \mathcal{E}_i \cup \mathcal{E}_D} \int_{E_i} [[v_h]] \cdot \left\{ \left\{ \frac{1}{\rho} \nabla u_h \right\} \right\} dE + \sum_{E_i \in \mathcal{E}_i \cup \mathcal{E}_D} \int_{E_i} \gamma [[u_h]] \cdot [[v_h]] dE. \end{aligned} \tag{2.5}$$

In (2.5), the three last terms correspond to the jumps and the fluxes of u_h through the edges of the elements. They obviously vanish when u_h and v_h belong to $H_0^1(\Omega)$, which occurs with classical finite element spaces where the approximate solution belongs to $H^1(\Omega)$ as the true solution.

The function γ , which penalizes the jump of u_h and v_h through the edges of \mathcal{T}_h is the so-called interior penalty function. It is defined on each edge $E \in \mathcal{E}_i \cup \mathcal{E}_D$ by: $\gamma|_E := \alpha c_{max} h_{min}^{-1}$ where α is a positive parameter independent of the mesh and c_{max} and h_{min} are defined by:

$$c_{max} = \begin{cases} \max(c_{|K^+}, c_{|K^-}), & \text{on } E \in \mathcal{E}_i, \\ c_{|K}, & \text{on } E \in \mathcal{E}_D; \end{cases} \quad h_{min|E} = \begin{cases} \min(h_K, h_{K'}), & \text{on } E \in \mathcal{E}_i, \\ h_K, & \text{on } E \in \mathcal{E}_D. \end{cases}$$

Then, according to [1], a_h is coercive if $\alpha > \frac{1}{2}l(l+1)$ when the mesh is uniform and composed of squares (in 2D) or cubes (in 3D). When the mesh is not uniform, or composed of triangles or tetrahedra, there exists α_0 such that a_h is coercive if $\alpha > \alpha_0$, but there is no explicit formula to determine α_0 . Moreover, the CFL condition of the fully discretized scheme decreases when α increases. It is then clear that we have to choose a penalization parameter greater than α_0 but as close as possible of α_0 . In practice, we use $\alpha_0 = 3$ for $l = 1$; $\alpha_0 = 5$ for $l = 2$; and $\alpha_0 = 10$ for $l = 3$.

Now, by considering a basis $(v_k)_{1 \leq k \leq N}$ of V_l^h , where N is the dimension of V_l^h , we get the linear system:

$$\mathcal{M} \frac{d^2 U_h}{dt^2} + \mathcal{B} \frac{d U_h}{dt} + \mathcal{K} U_h = G, \tag{2.6}$$

where

- U_h is the vector whose components are the coefficients of u_h in the basis (v_k) ;
- the matrix \mathcal{M} is the mass matrix which entries are defined by $\mathcal{M}_{ij} = \sum_{K \in \mathcal{T}_h} \int_K \frac{1}{\mu} v_i v_j$. This matrix is **block-diagonal**;
- the coefficients of matrix \mathcal{B} are defined by $\mathcal{B}_{ij} = b_h(v_i, v_j)$. Most of them vanish but the ones associated to degrees of freedom lying on the boundary Γ_{abs} . This matrix is also **block-diagonal**;
- the matrix \mathcal{K} is the stiffness matrix with coefficients defined by $\mathcal{K}_{ij} = a_h(v_i, v_j)$;
- G is the source vector defined by $G_i = \sum_{K \in \mathcal{T}_h} \int_K g v_i dx$.

All the integrals are **exactly computed** by a numerical quadrature of order at least l^2 . It is noteworthy that the approximate solution converges to the exact one with order $l+1$.

For the time discretization we use a classical second order centered scheme:

$$\mathcal{M} \frac{U_h^{n+1} - 2U_h^n + U_h^{n-1}}{\Delta t^2} + \mathcal{B} \frac{U_h^{n+1} - U_h^{n-1}}{2\Delta t} = -\mathcal{K} U_h^n + G_h^n. \tag{2.7}$$

This scheme is semi-explicit, since $\mathcal{M} + \frac{\Delta t}{2} \mathcal{B}$ is block diagonal and thus easily invertible.

In the following, we want to analyze the performance of the IPDGM when compared to the SEM and a FDM. For the SEM, we refer to the paper of Komatisch *et al.* [15] in which the reader can find information on the performance of the related space approximation method. Herein we want to compare these three approaches for two main reasons. First, the FDM is the easiest numerical method to handle and thus it is the most used in the world. Second, the SEM is based on finite element approximations. It is thus as flexible as the IPDGM to take the topography into account.

3 Performance analysis

In this section, we perform a comparison of IPDGM, SEM and FDM for a 2D case. The analysis of performance is done by considering a bilayered medium Ω composed of an upper layer $L_1 = [0; z_1] \times [0; x_1]$ and a lower layer $L_2 = [z_1; z_2] \times [0; x_1]$. The interface between L_1 and L_2 is flat and the propagation velocities are respectively denoted by c_1 in L_1 and c_2 in L_2 .

Herein, we have fixed the different parameters as follows:

$$z_1 = 16000\text{m}, \quad z_2 = 24470\text{m}, \quad x_1 = 21600\text{m}, \quad c_1 = 2400\text{ms}^{-1} \text{ et } c_2 = 1600\text{ms}^{-1}.$$

In practice, we use several sources g_j which are associated to a given point (x_j, z_j) as follows. As we already explained, the functions are defined by $g_j(x, z, t) = \delta_j(x, z)R(t)$. A suitable approximation $\delta_{j,h}$ of δ_j should satisfy $\int_{\Omega} \delta_{j,h} \phi = \phi(x_j, z_j)$ for each test function $\phi \in V_l^h$. Let K_j be the triangle such that $(x_j, z_j) \in K_j$. Then, $\delta_{j,h} = 0$ on each $K_l \in \mathcal{T}_h$, $l \neq j$. On K_j ,

$$\int_{K_j} \tilde{\delta}_{j,h}(x, z) \phi_l(x, z) = \phi_l(x_j, z_j)$$

for all basis functions ϕ_l which have a support in K_j . Let us remark that there is no need to compute the function $\delta_{j,h}$. It is indeed sufficient to set G_l to 0 if the support of ϕ_l does not include K_j and to $\phi_l(x_j, z_j)$ else. For the FDM, it is not possible to use this technique, and we consider that

$$g_j^s(x, z) = \begin{cases} h^{-2}, & \text{if } \|(x - x_j, z - z_j)\| \leq \frac{h}{2}, \\ 0, & \text{if } \|(x - x_j, z - z_j)\| > \frac{h}{2}. \end{cases}$$

Regarding the time dependency of the source, we have

$$R(t) = 2\pi^2 f_0^2 (2\pi^2 f_0^2 (t - 1/f_0)^2 - 1) e^{-\pi^2 f_0^2 (t - 1/f_0)^2},$$

where f_0 denotes the central frequency of the source.

To provide the comparison between the three methods, we have considered the case of only one source located to the point $(x_0, z_0) = (10300, 14470)$. The source will then begin

with generating waves in the upper layer L_1 and to measure the accuracy of the solution we compute the pointwise $L^2_{(x',z')}([0,T])$ relative error defined by:

$$e^h = \|u^h - u\|_{L^2_{(x',z')}([0,T])} = \frac{\sqrt{\int_0^T (u^h((x',z'),t) - u^{\text{ex}}((x',z'),t))^2 dt}}{\sqrt{\int_0^T (u^{\text{ex}}((x',z'),t))^2 dt}},$$

where u^h denotes the solution obtained either by IPDGM, SEM or FDM and u^{ex} is the exact solution obtained by the Cagniard-de Hoop method [2,10]. We used the $L^2_{(x',z')}([0,T])$ norm instead of the $L^2(\Omega \times [0; T])$ norm, which is most commonly computed in the literature. This is due to the fact that the computation of the exact solution by Cagniard-de Hoop method for all the points of the mesh and at all time steps of the simulation requires a very high computational burden.

The point $(x',z')=(15400,14470)$ has been chosen inside the computational box Ω and far enough from the boundary $\partial\Omega$ to be sure that $u^h(x',z',t)$ is not polluted by reflections created by $\partial\Omega$. Hence the relative error only measures the accuracy of the numerical scheme.

In the following experiments, the frequency f_0 is $f_0 = 2\text{Hz}$ and the final simulation time is $T = 16\text{s}$. We used P^3 elements on a triangular mesh with a mean space step h for the IPDGM; Q^3 elements on a regular quadrilateral mesh with a space step h for the SEM and a regular quadrilateral mesh with a space step h for the fourth order FDM. Hence, all the schemes are fourth order accurate in space. We decided to consider P^3 and Q^3 elements for the performance analysis since they are widely used in practice.

In Fig. 1 we represent the $L^2_{(x',z')}([0,T])$ norm provided by the three methods for various space steps h in logarithmic scale. The order of the three methods is two since we

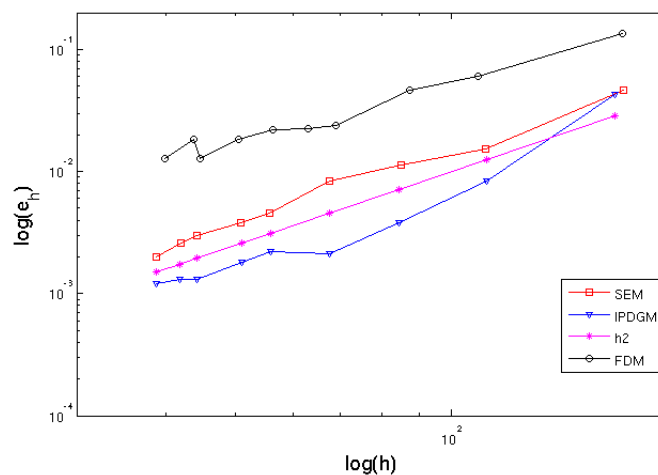


Figure 1: L^2 norm in logarithmic scale.

Table 1: Accuracy and computational burden of IPDGM in 2D.

Space discretization method	Number of elements	Number of degrees of freedom	CFL condition	Relative L^2 -error	Cost of one iteration	Total cost
IPDGM	14720	147200	6.3e-3	4.3e-2	5.9e6	1.5e10
	33600	336000	4e-3	8.3e-3	1.3e7	5.4e10
	58880	588800	3.1e-3	3.8e-3	2.4e7	1.2e11
	92000	920000	2.5e-3	2.1e-3	3.7e7	2.4e11
	162000	1620000	2e-3	1.8e-3	6.5e7	5.2e11
	239000	2390000	1.6e-3	1.3e-3	9.6e7	9.6e11
	280800	2808000	1.5e-3	1.2e-3	1.1e8	1.2e12

Table 2: Accuracy and computational burden of SEM in 2D.

Space discretization method	Number of elements	Number of degrees of freedom	CFL condition	Relative L^2 -error	Cost of one iteration	Total cost
SEM	15400	139351	9.6e-3	4.7e-2	3.5e6	5.8e9
	37400	337771	5.8e-3	1.5e-2	8.5e6	2.4e10
	64400	581131	4.8e-3	1.1e-2	1.5e7	4.9e10
	102000	919921	4.1e-3	8.3e-3	2.3e7	9e10
	180000	1622551	2.8e-3	3.8e-3	4.1e7	2.4e11
	264600	2384491	2.2e-3	2.6e-3	6e7	4.3e11
	310000	2793361	1.9e-3	2e-3	7e7	5.9e11

Table 3: Accuracy and computational burden of FDM in 2D.

Space discretization method	Number of elements	Number of degrees of freedom	CFL condition	Relative L^2 -error	Cost of one iteration	Total cost
FDM	n.a.	141899	9e-3	1.3e-1	1.3e6	2.3e9
		354011	5.6e-3	6.1e-2	3.1e6	9.1e9
		552286	4.7e-3	4.6e-2	5e6	1.7e10
		883225	3.6e-3	2.3e-2	7.9e6	3.5e10
		1655011	2.7e-3	1.9e-2	1.5e7	8.8e10
		2117520	2e-3	1.3e-2	1.9e7	1.5e11
		2646288	1.9e-3	1.2e-2	2.4e7	2e11

used a second order Leap-Frog scheme. Let us remark that the IPDGM is the most accurate for a given space step. However, the space step is not a good indicator of the computational burden and this figure does not provide enough information on the performances of the methods. Therefore, in Tables 1, 2 and 3, we present the number of degree of freedom, the $L^2_{(x',z')}([0,T])$ -relative error, the cost of one iteration and the total cost of the simulations. The cost of one iteration is the number of multiplications to be done at each time step. It corresponds to the number of non-zero elements in the matrix

Table 4: Comparison between the three methods for an accuracy of about 1%.

	IPDGM	SEM	FDM
Number of degrees of freedom	340000	920000	2700000
Total cost	5.4e10	9e10	2e11

$\mathcal{M}^{-1}\mathcal{K}$. The total cost of the simulations corresponds to the cost of one iteration multiplied by the number of iterations.

Tables 1, 2 and 3 reveal that, for a prescribed number of degrees of freedom, IPDGM improves the accuracy by a factor 2 (resp. 4) compared to SEM (resp. FDM), whereas the computational cost of IPDGM is twice (resp. ten times) the one of SEM (resp. FDM). However, this conclusion does not reflect correctly the performances of the three methods. Indeed, we need to compare the computational cost of the methods for a prescribed level of accuracy (or the level of accuracy for a prescribed computational cost). Therefore, we present in Table 4 the computational cost needed by the three methods to achieve a level of accuracy of 1%. The computational cost of SEM (resp. FDM) is twice (resp. four times) the cost of IPDGM. Moreover SEM (resp. FDM) requires twice (resp. 8 times) the number of degrees of freedom required by IPDGM. The performances of IPDGM compared to SEM are also better for other levels of accuracy (compare for instance the results in Tables 1 and 2 for an accuracy of 0.2%).

4 One example of application to the Reverse Time Migration

In this section, we present an example of a heterogeneous environment that we obtained using the RTM when the acoustic wave equation is solved in a IPDG formulation. The velocity model we consider is an interesting test case because it represents layers of variable geometry in which the velocities vary widely. In particular, the medium has a salt dome (see in Fig. 2, the area where the speed is 5500 m/s) which is very important to correctly image. Indeed, pockets of hydrocarbons are often hidden beneath the salt-bearing areas.

4.1 General setting

As all the migration techniques, RTM follows the Claerbout's schedule which we briefly describe in the following. We denote by $f_j(x,z,t)$ the sources used during the acquisition campaign and by $r_j(x,z,t)$ the signal recorded at the receivers for each source during the same acquisition campaign. Then an iteration of RTM is composed of the three following steps.

1. Firstly, we reproduce numerically the acquisition campaign: using the same sources, the wavefield is created by modelling the propagation of the waves during a time

slot T . The resulting wavefield is denoted by U_j^s and it is solution to the problem:

$$\left\{ \begin{array}{ll} \frac{1}{\mu} \frac{\partial^2 U_j^s}{\partial t^2} - \nabla \cdot \left(\frac{1}{\rho} \nabla U_j^s \right) = f_j(\cdot, t), & \text{in }]0, T[\times \Omega, \\ U_j^s = 0, & \text{on }]0, T[\times \Gamma_D, \\ \frac{1}{\sqrt{\mu}} \frac{\partial U_j^s}{\partial t} + \frac{1}{\sqrt{\rho}} \nabla U_j^s \cdot \mathbf{n} = 0, & \text{on }]0, T[\times \Gamma_{abs}, \\ U_j^s(x, z, 0) = 0, \frac{\partial U_j^s}{\partial t}(x, z, 0) = 0, & \text{in } \Omega. \end{array} \right.$$

- Secondly, we reconstruct the reflected wavefield recorded by the receivers. We perform a retropropagation of the receivers' data by computing the wavefield generated by the recorded signals r_j between T and 0 . This step can be performed accounting for the time reversibility of the wave equation in Ω . The resulting wavefield is denoted by U_j^r and it is the solution to the problem:

$$\left\{ \begin{array}{ll} \frac{1}{\mu} \frac{\partial^2 U_j^r}{\partial t^2} - \nabla \cdot \left(\frac{1}{\rho} \nabla U_j^r \right) = r_j(\cdot, T_f t), & \text{in }]0, T[\times \Omega, \\ U_j^r = 0, & \text{on }]0, T[\times \Gamma_D, \\ \frac{1}{\sqrt{\mu}} \frac{\partial U_j^r}{\partial t} + \frac{1}{\sqrt{\rho}} \nabla U_j^r \cdot \mathbf{n} = 0, & \text{on }]0, T[\times \Gamma_{abs}, \\ U_j^r(x, z, 0) = 0, \frac{\partial U_j^r}{\partial t}(x, z, 0) = 0, & \text{in } \Omega. \end{array} \right.$$

- Finally, we construct the image by applying an imaging condition, which consists in correlating the sources and the receivers wavefields. A strong coefficient corresponds then to a reflector. The imaging condition that we used is given by [4]:

$$I(x, z) = \sum_{j=1}^N \int_0^{T_f} U_j^s(x, z, t) \cdot U_j^r(x, z, t) dt,$$

where N is the number of sources.

4.2 Results

We show here a 2D RTM result involving the fourth order IPDGM. We consider a complex media $[0, 15000] \times [0, 5000]$ with an irregular surface and different zones where the velocity is $c_1 = 2500 \text{ms}^{-1}$, $c_2 = 2700 \text{ms}^{-1}$, $c_3 = 3000 \text{ms}^{-1}$, $c_4 = 3500 \text{ms}^{-1}$, $c_5 = 4000 \text{ms}^{-1}$, $c_6 = 4500 \text{ms}^{-1}$ or $c_7 = 5500 \text{ms}^{-1}$ as shown in the Fig. 2. We use 100 sources with frequency $f_0 = 10 \text{Hz}$ and 500 receivers. The positions of sources are represented by the green triangles on Fig. 2 they are buried 10 meters below the surface and regularly spaced by 125

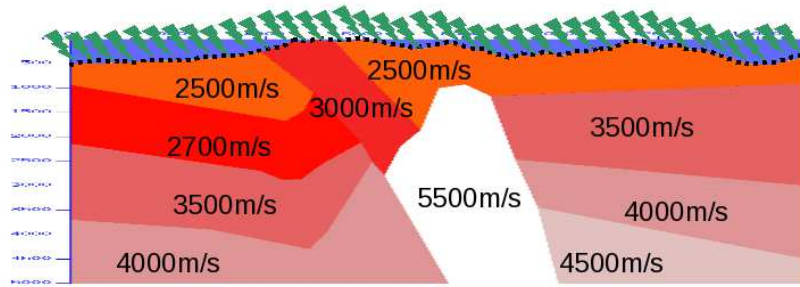


Figure 2: Description of the experiment.

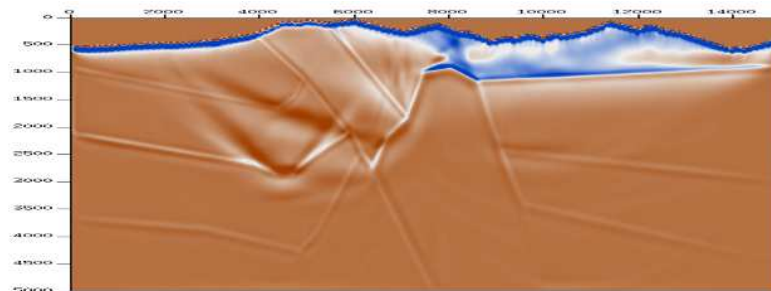


Figure 3: Final image with IPDGM

meters. The receivers are also buried 10 meters below the surface and regularly spaced by 25 meters. We impose a Dirichlet boundary condition on the top of the domain and an absorbing boundary condition elsewhere. The time of the simulation is 4s. This example is relevant because, on the one hand, the velocity medium includes a salt dome (high-contrasts of velocity) and, on the other hand, the topography effects are taken into account.

The final image is depicted in Fig. 3 and we can see that we recover all the interfaces into the domain. To obtain this image, we used a mesh composed of 45 000 elements and 450 000 degrees of freedom. We reproduced this experiment with a Finite Difference Method and to obtain an image similar to the one depicted in Fig. 3, we had to use a grid composed of 4 700 000 points, which is about ten times higher than the number of points we used with IPDGM.

5 Conclusion

The numerical comparisons we have carried out show that the IPDGM performs at least as well as the SEM for solving the acoustic wave equation. Since the IPDGM allows for the use of triangular and tetrahedral meshes, which are more adapted to complex topographies, we have chosen to apply this method to the RTM. The numerical results

we have presented illustrate the fact that IPDGM is indeed well adapted to this kind of problem. Another advantage of the IPDGM, as compared to the SEM, is its capability to deal with non-conforming meshes containing locally-refined cells and/or cells of various order. In a forthcoming work, we will show how this property, combined with a local time stepping strategy, can improve the performances of the RTM.

Acknowledgments

The authors acknowledge the support by TOTAL/INRIA strategic action DIP (Depth Imaging Partnership).

References

- [1] M. Ainsworth, P. Monk, and W. Muniz. Dispersive and dissipative properties of discontinuous galerkin finite element methods for the second-order wave equation. *J. Sci. Comput.*, 27(1-3), 2006.
- [2] L. Cagniard. *Reflection and Refraction of Progressive Seismic Waves*. McGraw-Hill, 1962.
- [3] P.G. Ciarlet. *The Finite Element Method for Elliptic Problems*. North-Holland Publishing Co., Amsterdam, 1978. *Studies in Mathematics and its Applications*, Vol. 4.
- [4] J.F. Claerbout. Toward a unified theory of reflector imaging. *Geophysics*, 36:467–481, 1971.
- [5] G. Cohen, P. Joly, J. E. Roberts, and N. Tordjman. Higher order triangular finite elements with mass lumping for the wave equation. *SIAM J. Numer. Anal.*, 38(6):2047–2078 (electronic), 2001.
- [6] G. Cohen, P. Joly, and N. Tordjman. Construction and analysis of higher order finite elements with mass lumping for the wave equation. In *Second International Conference on Mathematical and Numerical Aspects of Wave Propagation* (Newark, DE, 1993), pages 152–160. SIAM, Philadelphia, PA, 1993.
- [7] G. Cohen, P. Joly, and N. Tordjman. Higher-order finite elements with mass-lumping for the 1D wave equation. *Finite Elem. Anal. Des.*, 16(3-4):329–336, 1994. ICOSAHOM '92 (Montpellier, 1992).
- [8] J. D. De Basabe and M. K. Sen. New developments in the finite-element method for seismic propagation simulation. *Leading Edge*, 28:562–567, 2009.
- [9] J. D. De Basabe and M. K. Sen. Stability of the high-order finite elements for acoustic or elastic wave propagation with high-order time stepping. *Geophys. J. Int.*, 181:577–590, 2010.
- [10] A. T. de Hoop. The surface line source problem. *Appl. Sci. Res. B*, 8:349–356, 1959.
- [11] J. Gazdag. Wave equation migration with the phase-shift method. *Geophysics*, 43(7):1342–1351, December 1978.
- [12] M.J. Grote, A. Schneebeli, and D. Schözu. Discontinuous Galerkin finite element method for the wave equation. *SIAM J. Numer. Anal.*, 44(6):2408–2431 (electronic), 2006.
- [13] T.J.R. Hughes. *The finite element method*. Prentice Hall Inc., Englewood Cliffs, NJ, 1987. *Linear static and dynamic finite element analysis*, With the collaboration of Robert M. Ferencz and Arthur M. Raefsky.
- [14] J. Gazdag J and P. Sguazzero. Migration of seismic data by phase shift plus interpolation. *Geophysics*, 49(2):124–131, February 1984.

- [15] D. Komatitsch and J. Tromp. Introduction to the spectral element method for three-dimensional seismic wave propagation. *Geophys. J. Int.*, 139:806–822, 1999.
- [16] D. Komatitsch, J-P. Vilotte, R. Vai, J.M. Castillo-Covarrubias, and F.J. Sanchez-Sesma. The spectral element method for elastic wave equations: application to 2d and 3d seismic problems. *Int. J. Num. Methods Engr.*, 45:1139–1164, 1999.
- [17] D. Komatitsch and J.P. Vilotte. The spectral-element method: An efficient tool to simulate the seismic response of 2d and 3d geological structures. *Bulletin of the Seismological Society of America*, 88(2):368–392, 1998.
- [18] P.L. Stoffa, R.M Fokkema, W.P. de Luna Freire, and Kessinger. Split-step fourier migration. *Geophysics*, 55(4):410–421, April 1990.